





Cite this: *Dalton Trans.*, 2022, **51**,
3625

Preparation of water-dispersible Janus nanosheets from $K_4Nb_6O_{17}\cdot 3H_2O$ and their behaviour as a two-dimensional surfactant on air–water and water–toluene interfaces†

Ryoko Suzuki, ^{a,b} Tomoki Nagai,^a Emika Onitsuka,^c Naokazu Idota, ^{b,d}
Masashi Kunitake, ^e Taisei Nishimi^f and Yoshiyuki Sugahara ^{*a,b}

$K_4Nb_6O_{17}\cdot 3H_2O$ -based Janus nanosheets with water dispersibility and surface activity were prepared via sequential regioselective surface modification. To provide individual Janus nanosheets with these two properties, phenylphosphonic acid and phosphoric acid were utilized for surface modification at interlayers I and II of $K_4Nb_6O_{17}\cdot 3H_2O$, respectively, and the resulting product was exfoliated into single-layered nanosheets by ultrasonication in water. The resulting aqueous dispersion of the Janus nanosheets showed lower surface tension than pure water, confirming that the Janus nanosheets had surface activity. An o/w emulsion was formed using the Janus nanosheet aqueous dispersion and toluene. In this emulsion, characteristic phenomena, coalescence and Ostwald ripening behaviour of toluene droplets were observed; the appearance of ellipsoidal droplets during coalescence and a rapid Ostwald ripening which differ from those observed for systems using conventional surfactants, were observed. These phenomena likely originated from the unique anisotropic structures of Janus nanosheets with their nm-scale thickness and μm -range lateral size.

Received 28th October 2021,
Accepted 28th January 2022

DOI: 10.1039/d1dt03647e

rsc.li/dalton

Introduction

Janus materials with two properties on the two surfaces of each piece are expected to be applied as catalysts,¹ optical materials² and surfactants³ due to their unique structures. Janus nanomaterials with various shapes, such as nanoparticles, nanorods and nanosheets, have been prepared,^{4,5} and Janus nanosheets exhibit the highest anisotropy among Janus nanomaterials. Surfactants have been considered to be one of the most effective applications of Janus nanosheets,

because “flip-flop” rotation at interfaces is restricted for Janus nanosheets⁶ compared to Janus nanoparticles and their adsorption energy to air–liquid or an oil–water interfaces is higher.^{7–9} The use of inorganic Janus nanosheets is preferable for application as two-dimensional surfactants, since solvent molecules hardly penetrate into inorganic Janus nanosheets as one characteristic differentiating them from those of polymer-based Janus nanosheets.

Not only general low-molecular-weight surfactants but also amphiphilic polymers and macromolecules are known to exhibit surface activity.¹⁰ These polymeric surfactants efficiently stabilize emulsions, since they can selectively adsorb onto water–oil interfaces.¹¹ Surface activities have been found for various solid particles, moreover, including hydrophobic silica, clay minerals, carbon black, and latex,¹² and they have been utilized for preparing Pickering emulsions which are stabilized by solid particles adsorbed at the liquid–liquid interface.¹³

Janus nanoparticles with individual hydrophobic and hydrophilic surfaces also exhibited surface activity. Gold,¹⁴ silica,^{15,16} and block copolymers¹⁷ based Janus nanoparticles showed surface activity and a stabilized emulsion. In the history of surfactants, Janus nanosheets are attracting attention as a new category of surfactants due to their unique two-dimensional structures. It should be worth noting that Janus nanosheets possess ultra-thin layered structures and wide

^aDepartment of Applied Chemistry, School of Advanced Science and Engineering, Waseda University, 3-4-1, Okubo, Shinjuku-ku, Tokyo 169-8555, Japan.
E-mail: ys6546@waseda.jp

^bKagami Memorial Research Institute for Science and Technology, Waseda University, 2-8-26, Nishiwaseda, Shinjuku-ku, Tokyo 169-0051, Japan

^cTechnical Division, Kumamoto University, 2-39-1, Kurokami, Chuo-ku, Kumamoto 860-8555, Japan

^dLaboratory for Zero-Carbon Energy, Institute of Innovative Research, Tokyo Institute of Technology, 2-12-1-N1-6, O-okayama, Meguro-ku, Tokyo 152-8550, Japan

^eInstitute of Industrial Nanomaterials, Kumamoto University, 2-39-1, Kurokami, Chuo-ku, Kumamoto 860-8555, Japan

^fJapan Technological Research Association of Artificial Photosynthetic Chemical Process (ARPCHEM), Room 422, Bldg. 12, Faculty of Engineering, The University of Tokyo, 2-11-16 Yayoi, Bunkyo-ku, Tokyo 113-8656, Japan

† Electronic supplementary information (ESI) available: Contact angle, optical microscopic images and a movie of emulsion. See DOI: 10.1039/d1dt03647e



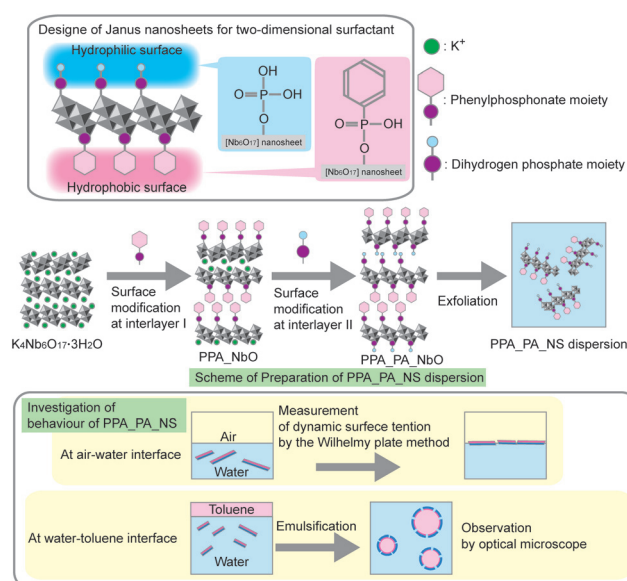
lateral sizes, typically with submicron meter range, could also have a hydrophilic surface and a hydrophobic surface.

Use of various Janus nanosheets and nanoplates as two-dimensional surfactants has been reported.^{18–23} Silica-based Janus nanosheets were prepared by crashing hollow silica spheres with one type of functional group on their inner surface and the other type on their outer surface.^{18–21} Ji *et al.* prepared silica-based Janus nanosheets with hydrophobic groups and ionic liquid (imidazolium) moieties and demonstrated the control of hydrophilicity of ionic liquid moieties by exchange of counterions.¹⁹ Emulsions using water and one of several organic solvents were also prepared using the aforementioned Janus nanosheets.²⁰ Oil droplets with irregular shapes were observed in these emulsions, and their formation was ascribed to the increasing viscosity of a continuous water phase caused by the presence of dispersed Janus nanosheets, and to the aggregation of Janus nanosheets at the oil–water interfaces on the droplet surfaces. Janus nanosheets with hydrophobic acryloyl groups and hydrophilic Si–OH groups were also reported.²¹ An emulsion consisting of water and toluene using the Janus nanosheets as a surfactant exhibited higher stability than an emulsion using a conventional cetyltrimethylammonium bromide surfactant. It was considered that the emulsion was stabilized partly by limiting rotation of the Janus nanosheets on toluene droplet surfaces. Graphene-based Janus nanosheets also behaved as a two-dimensional surfactant.²² One side of each graphene oxide (GO) nanosheet was modified with octadecylamine by electrostatic interaction at the interface of water and kerosene for preparation of the Janus nanosheets. The Janus nanosheets exhibited amphiphilicity, and surfaces bearing octadecylamine were adsorbed on heptane at the interface of water and heptane. In addition, preparation of MXene-based Janus nanosheets and their two-dimensional surfactant behaviour were reported.²³ One side of each MXene nanosheet with a negative charge was modified with positively charged polystyrene chains. The 0.03 wt% aqueous dispersion of these Janus nanosheets decreased the water–toluene interfacial tension to 30–35 mN m⁻¹. Although it has been confirmed that Janus nanosheets acted as two-dimensional surfactants, their surface and interfacial behaviour has not been sufficiently studied. Halloysite-based Janus nanoplates which were prepared *via* two step surface modification also stabilized an emulsion.²⁴ Halloysite consists of nanoplates with an alumina side and a silica side. First, the alumina side was modified using phenyl phosphonic acid that could not react with the silica side to form a hydrophobic surface. Then, the silica side was modified with poly(dimethylamino ethyl methacrylate) by surface-initiated atom transfer radical polymerization to form a hydrophilic surface. The resulting Janus nanoplates decreased interface tension between dodecane and water and stabilized an o/w emulsion.

We have developed K₄Nb₆O₁₇·3H₂O-based Janus nanosheets using its unique structure and the resulting intercalation chemistry of K₄Nb₆O₁₇·3H₂O, where interlayer I with high reactivity and interlayer II with low reactivity appear alternately in the stacking direction. First, interlayer I was expanded by intro-

ducing an appropriate bulky ammonium ion to produce an “A-type” intercalation compound where guest species are present only at interlayer I. This A-type intercalation compound was then reacted with organophosphonic acid for surface modification at interlayer I to form an A-type derivative. Interlayer II of the A-type derivative was further expanded using another less bulky ammonium ion, and the resulting intercalation compound was reacted with another organophosphonic acid for surface modification at interlayer II. The product was exfoliated by ultrasonication, and a Janus nanosheet dispersion was obtained. It should be noted that stable Nb–O–P bonds are present between the niobite nanosheet surface and surface functional groups, which is very advantageous for their use as a two-dimensional surfactant. These K₄Nb₆O₁₇·3H₂O-based Janus nanosheets furthermore exhibit versatility in the selection of surface functional groups achieved by changing the surface modifiers,²⁵ and one type of K₄Nb₆O₁₇·3H₂O-based Janus nanosheets bearing hydrophilic and hydrophobic groups was reported. It is therefore expected that another type of K₄Nb₆O₁₇·3H₂O-based Janus nanosheets with appropriate hydrophilicity and hydrophobicity on opposite sides of the individual nanosheets for their stable dispersion in water can be prepared by proper selection of surface modifiers and behaves as a two-dimensional surfactant.

Here we report the preparation of K₄Nb₆O₁₇·3H₂O-based single-layered Janus nanosheets with one surface modified by phenylphosphonic acid and the other with phosphoric acid. These Janus nanosheets could be dispersed in water by increasing their hydrophilicity compared to the Janus nanosheets reported in our previous study,²⁵ which have octadecylphosphonate moiety and carboxypropylphosphonate moiety on the opposite surfaces of each nanosheet. In order to clarify their surfactant behaviour, the nanosheets' surface behaviour at the air–water interface was investigated by



Scheme 1 Preparation and investigation of behaviour of PPA_PA_NS.



dynamic surface tension measurement. An o/w emulsion was prepared using an aqueous dispersion of the obtained Janus nanosheets and toluene, moreover, and their interfacial behaviour at the water–toluene interface was investigated by continuous optical microscopic observation (Scheme 1).

Experimental section

Materials

K_2CO_3 (Wako Pure Chemical Ind. Co.) and Nb_2O_5 (Wako Pure Chemical Ind. Co.) were used for preparation of $K_4Nb_6O_{17} \cdot 3H_2O$. Dimethyldioctadecylammonium chloride (FUJIFILM Wako Pure Chemical Co.) and dodecylammonium chloride ($C_{12}NCl$, Tokyo Chemical Industry Co., Ltd) were used for preparation of intermediates for surface modification. Phenylphosphonic acid (PPA, Tokyo Chemical Industry Co., Ltd) and phosphoric acid (PA, Tokyo Chemical Industry Co., Ltd) were used as surface modifiers for interlayers I and II, respectively. For surface modification, 2-butanone (FUJIFILM Wako Pure Chemical Co., Ltd) was used as a dispersing medium for surface modification. Toluene (FUJIFILM Wako Pure Chemical Co., Ltd) was used for preparing an emulsion, and oil orange (Tokyo Chemical Industry Co., Ltd) was used to colourise an oil phase.

Experimental procedures

Preparation of $K_4Nb_6O_{17} \cdot 3H_2O$. $K_4Nb_6O_{17} \cdot 3H_2O$ was prepared by calcination of a mixture of K_2CO_3 (2.83 g, 2.05×10^{-2} mol) and Nb_2O_5 (7.43 g, 2.80×10^{-2} mol) at 1100 °C for 10 hours without intermittent grinding. The product was washed with water and dried in air.

Preparation of PPA_NbO.²⁶ $K_4Nb_6O_{17} \cdot 3H_2O$ (2.60 g, 2.50×10^{-3} mol) and dimethyldioctadecylammonium chloride (5.87 g, 1.00×10^{-2} mol, $K_4Nb_6O_{17} \cdot 3H_2O$ to dimethyldioctadecylammonium chloride molar ratio was 1:4) were reacted in water (200 mL) at 50 °C for 7 days to expand interlayer I. The intermediate was centrifuged, washed with water and dried in air. Next, the product (1.0 g) and PPA (0.90 g, 5.7×10^{-3} mol, Nb_6O_{17} to PPA molar ratio was 1:4) were added to 2-butanone (40 mL) and reacted at 80 °C for 1 day to modify the surface of interlayer I. This reaction was repeated four times. The product was washed twice with hydrochloric acid (pH = 3) and three times with acetone. Then the product was air-dried (PPA_NbO).

Preparation of PPA_PA_NbO. PPA_NbO (0.10 g) and $C_{12}NCl$ (0.23 g, 1.0×10^{-3} mol, Nb_6O_{17} to $C_{12}NCl$ molar ratio 1:10) were reacted in water (20 mL) at 80 °C for 3 days to expand interlayer II as described in our previous report.²⁴ The intermediate, PPA- $C_{12}N$ -NbO, was centrifuged and washed with water three times and dried in air. The intermediate (0.20 g) and PA (0.056 g, 5.7×10^{-4} mol, Nb_6O_{17} to PA molar ratio was 1:4) were reacted in 2-butanone (40 mL) at 50 °C for 1 day under an N_2 atmosphere. This reaction was repeated four times. Finally, the product was washed with acetone three times and dried in air (PPA_PA_NbO).

Preparation of a PPA_PA_NbO_NS aqueous dispersion. PPA_PA_NbO (100 mg) was dispersed in water (100 mL), stirred overnight and sonicated for exfoliation. Ultrasonication was carried out for 2 h (with a 2 s interval for every 2 s irradiation) in an ice bath using a BRANSON Advanced Digital Sonifier. The obtained dispersion was then centrifuged at 4500 rpm for 15 min, and the supernatant was collected (PPA_PA_NS aqueous dispersion).

Preparation of an emulsion using PPA_PA_NbO_NS aqueous dispersion and toluene. An emulsion was prepared using a PPA_PA_NS aqueous dispersion and toluene coloured with oil orange as a water phase and an oil phase, respectively. The PPA_PA_NS aqueous dispersion (10 mL) and toluene (0.2 mL) were mixed in a test tube using a homogenizer (IKA ULTRA-TURRAX® T18 digital) for 1 min at 15 000 rpm.

Analyses. X-ray diffraction (XRD) patterns were recorded on a Rigaku RINT-1000 diffractometer (Mn-filtered Fe K α radiation). Solid-state ^{31}P NMR spectra were obtained with a magic angle spinning (MAS) technique only (pulse delay, 30 s; spinning rate, 12 kHz) using a JEOL JNM-ECX 400 spectrometer at 160.26 MHz. Triphenylphosphine (−8.4 ppm) was used as an external standard for solid-state ^{31}P MAS NMR. Solid-state ^{13}C cross-polarization (CP)/MAS NMR spectra were also obtained using a JEOL JNM-ECX-400 spectrometer at 99.55 MHz (pulse delay, 5 s; contact time, 1.5 ms; spinning rate, 12 kHz). Hexamethylbenzene (17.4 ppm) was used as an external standard for the solid-state ^{13}C CP/MAS NMR. Inductively coupled plasma emission spectrometry was performed with a Thermo Jarrell Ash ICAP-574 II instrument by the internal standard method after dissolution of the sample overnight in a mixture of 4 mL of HNO_3 , 3 mL of HCl , and 1 mL of HF at 150 °C. A transmission electron microscopic (TEM) image was obtained using a JEOL JEM-1011 microscope operated at 100 kV. For the electron diffraction (ED) analysis, the incident electron beam was perpendicular to the lateral plane of the nanosheets. TEM and ED samples were prepared by casting a nanosheet dispersion on the grid and decompression drying. Atomic force microscopic (AFM) images were obtained with a Digital Instruments Nanoscope III using the tapping mode. The surface tension was measured by the Wilhelmy plate method using a Kyowa DY-300 instrument at room temperature. Image analysis of the emulsion was carried out using an Image J (Wayne Rasband (NIH)) optical microscope and the sphericity was calculated as $4\pi \times$ (area of sphere/square of circumference).

Results and discussion

Preparation of a Janus nanosheet dispersion

The organic moieties in the products were investigated by solid-state ^{13}C CP/MAS NMR. Fig. 1 shows ^{13}C CP/MAS NMR spectra of PPA_NbO and PPA_PA_NbO. Broad signals assignable to phenyl groups were observed at 128 and 131 ppm in the spectrum of PPA_NbO (Fig. 1a),²⁶ indicating the presence of PPA moiety in PPA_NbO. Broad signals at 128 and 131 ppm



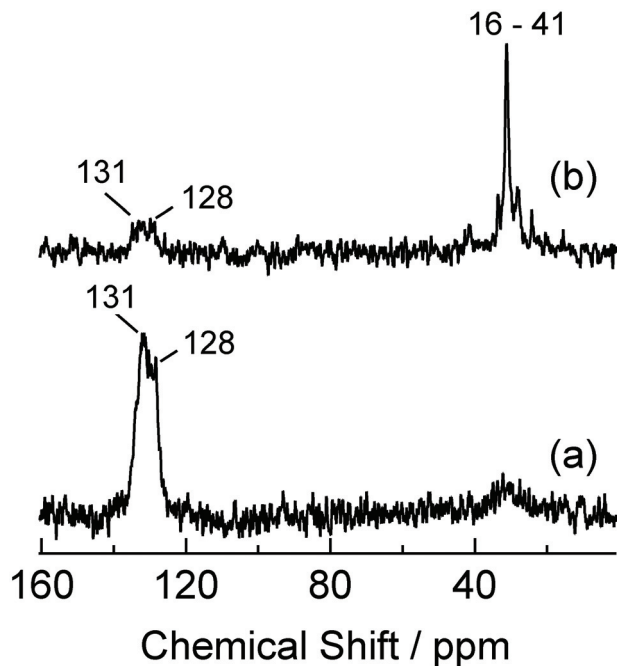


Fig. 1 Solid-state ^{13}C CP/MAS NMR spectra of (a) PPA_NbO and (b) PPA_PA_NbO.

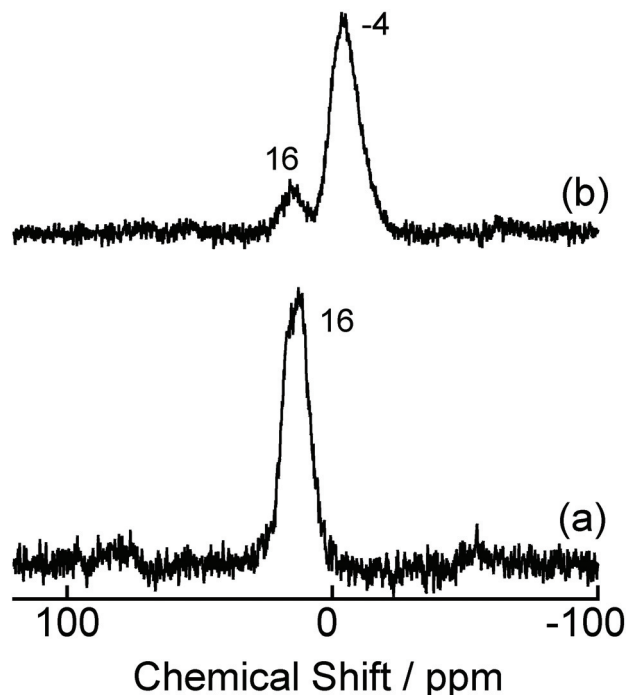


Fig. 2 Solid-state ^{31}P MAS NMR spectra of (a) PPA_NbO and (b) PPA_PA_NbO.

were also observed in the spectrum of PPA_PA_NbO (Fig. 1b), indicating maintenance of the PPA moiety. Furthermore, weak signals assignable to *n*-dodecyl chains in C_{12}N^+ were observed at 16–41 ppm, a result indicating the presence of C_{12}N^+ in PPA_PA_NbO.²⁵

Since PA has no organic moiety, sequential surface modifications can be monitored using solid-state ^{31}P MAS NMR. Fig. 2 shows solid-state ^{31}P MAS NMR spectra of the products. In the spectrum of PPA_NbO (Fig. 2a), a signal assignable to a PPA moiety was observed, which is consistent with the ^{13}C CP/MAS NMR result showing the presence of phenyl groups. The ^{31}P NMR signal was shifted upfield from that of the PPA molecule (22 ppm)²⁶ to 16 ppm, indicating formation of Nb–O–P bonds between the niobate nanosheet surface and PPA moieties.²⁶ This result confirms that a hydrophilic PPA moiety was immobilized on the niobate layers. In the spectrum of PPA_PA_NbO (Fig. 2b), two signals were observed at 16 ppm and –4 ppm. The presence of a signal at 16 ppm confirms that Nb–O–P bonds were maintained between the niobate nanosheets and PPA moieties. Also, the other signal was assignable to a PA moiety grafted onto the niobate layer. In previous reports, a PA moiety grafted onto Nb_2O_5 showed a signal at –3 ppm, which shifted upfield from that of the PA molecule (0 ppm) by 3 ppm.²⁷ In the case of surface modification of $\text{HLaNb}_2\text{O}_7 \cdot x\text{H}_2\text{O}$ layered materials with oleyl phosphate, an ester of PA, a similar upfield shift was observed.²⁸ It is therefore concluded that Nb–O–P bonds were additionally formed between the PA moiety and niobate layer. Based on our previous study using the same set of alkylammonium ions for preparing intermediates,²⁵ it can be concluded that PPA and

PA moieties were mobilized in interlayers I and II by two-step surface modification. Based on our previous study on interlayer surface modification of $\text{K}_4\text{Nb}_6\text{O}_{17} \cdot 3\text{H}_2\text{O}$ by PPA, both PPA and moieties should be present in $\text{PhP}(\text{O})(\text{OH})\text{O-Nb}$ and/or $(\text{HO})_2\text{P}(\text{O})\text{O-Nb}$ monodentate environments.²⁶

Then, the amounts of PPA and PA moieties as well as of $2\text{C}_{18}2\text{MeN}^+$ and C_{12}N^+ alkylammonium ions at interlayers I and II in the products were estimated based on the ICP and CHN results (Table 1). It should be noted that the amounts of PPA and PA in PPA_PA_NbO are the important pieces of information for determining whether PPA_PA_NbO can be converted into “Janus” nanosheets by exfoliation. In PPA_NbO, which is estimated to be an A-type derivative, the Nb : P molar ratio was calculated to be 6.0 : 1.9. Since the molar ratio for the maximum modification amount of guest species in interlayer I is equal to the molar ratio of potassium in interlayer I, Nb : P = 6.0 : 2.0,²⁵ 95% of the reactive sites in interlayer I of PPA_NbO were modified with PPA. In PPA_NbO, no N atoms were present, indicating complete removal of $2\text{C}_{18}2\text{MeN}^+$ from

Table 1 The molar ratios of Nb, P and N

	Nb/—	P/—	N/—
PPA_NbO	6.0	1.9	0
PPA_C ₁₂ N_NbO ^a	6.0	1.9	1.5
PPA_PA_NbO	6.0	3.4	0.9

^a PPA_C₁₂N_NbO was prepared by intercalation of C_{12}N^+ in PPA_NbO as a precursor of PPA_PA_NbO.



interlayer I of PPA_NbO. In PPA_C₁₂N_NbO, molar ratio of P to Nb did not decrease from that of the PPA_NbO, indicating maintenance of PPA moiety in interlayer I. Also, nitrogen was detected in PPA_C₁₂N_NbO, suggesting that C₁₂N⁺ ions were introduced in PPA_C₁₂N_NbO. After the PA treatment (PPA_PA_NbO), the Nb:P molar ratio was calculated as 6.0:3.4, indicating that the relative molar ratio of P increased by 1.5 (per 6 Nb) from PPA_C₁₂N_NbO. Since the molar ratio corresponding to the maximum modification amounts of guest species in interlayers I and II are both Nb:P = 6.0:2.0,²⁵ it is considered that the possible molar amounts of the modified PA moieties relative to 6 Nb are in the ranges of 0–0.1 (0%–5%) in interlayer I and 1.4–1.5 (70%–75%) in interlayer II. From these results, it was concluded that interlayer I was modified mainly with the PPA moieties, while interlayer II was modified only with the PA moieties. On the other hand, molar ratio of Nb:N was 6.0:1.0 which decreased from Nb:N = 6.0:1.5, indicating removal of a part of C₁₂N⁺ from PPA_PA_NbO.

Based on these results, it was concluded that PPA_PA_NbO had largely different modification ratios of PPA and PA in interlayers I and II. Thus, the stacking structure of PPA_PA_NbO is discussed using the XRD results. XRD patterns of PPA_NbO and PPA_PA_NbO (Fig. 3) showed the *d* values corresponding to the repeating distances, 2.90 nm and 3.62 nm, respectively. The repeating distance of PPA_NbO was closely similar to that of A-type PPA_NbO in our previous study.²⁶ Assuming that PPA_PA_NbO is also an A-type derivative, where two different interlayers appear alternately in the stacking direction,²⁵ the repeating distance is calculated to be

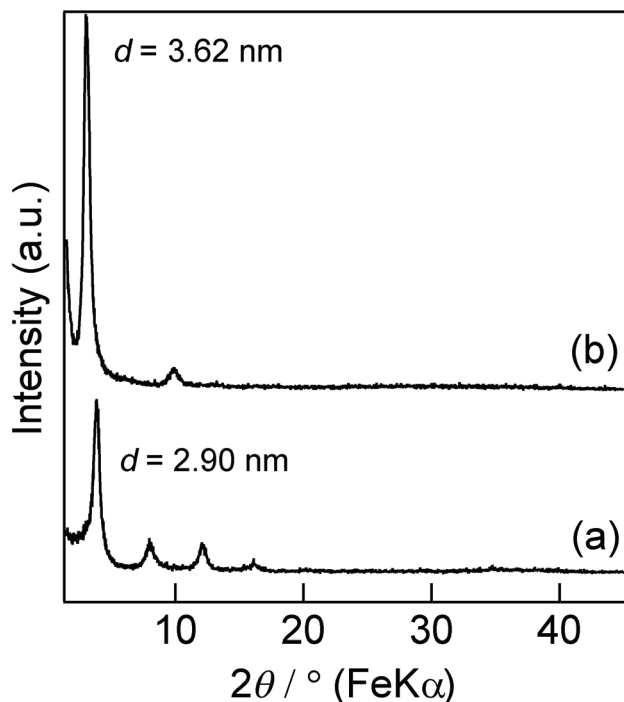


Fig. 3 XRD patterns of (a) PPA_NbO and (b) PPA_PA_NbO.

3.60 nm, that is a doubled sum of the sizes of the PPA moiety, 0.63 nm,¹⁷ PA moiety, 0.35 nm and the thickness of a [Nb₆O₁₇]⁴⁻ nanosheet, 0.82 nm;²⁹ (0.63 nm + 0.35 nm + 0.82 nm) × 2 = 3.60 nm. As discussed above, PA moieties relative to 6 Nb are in the ranges of 0–0.1 (0%–5%) in interlayer I and 1.4–1.5 (70%–75%) in interlayer II. If PA:Nb = 0:6 in interlayer I, PPA and PA are present only in interlayers I and II, respectively. If PA:Nb = 0.1:6 in interlayer I, interlayer I has a PPA moiety and PA moiety and interlayer II has only a PA moiety. In either case, the thickness of interlayer I should be determined only by the size of the PPA moiety, since the PPA moiety is larger than the PA moiety. The repeating distance of PPA_PA_NbO should therefore be independent of the amount of the PA moiety in interlayer I. Thus, the observed repeating distance of PPA_PA_NbO, 3.62 nm, a value closely similar to the calculated value, indicates that PPA_PA_NbO was an A-type derivative.

Fig. 4 shows SEM images of K₄Nb₆O₁₇·3H₂O, PPA_NbO and PPA_PA_NbO. All of them show plate-like shapes of similar lateral sizes, about 60 μm, suggesting that all reactions proceeded with maintenance of the shape of K₄Nb₆O₁₇·3H₂O.

Based on these data, the reaction seemed to proceed through the following steps. First, surface modification using PPA at interlayer I was achieved by using the A-type intercalation compound described in our previous report; an A-type organophosphonate derivative can be obtained from an A-type intercalation compound, since organophosphonic acid reacted only at interlayers expanded by ammonium ions.²⁶ PPA_NbO was further reacted with C₁₂N⁺ ions, and the following PA treatment of this product provided PPA_PA_NbO, which should also be an A-type derivative; interlayer II was expanded by intercalation of C₁₂N⁺ and subsequently modified by PA with maintaining the stacking regularity. In our previous report on preparation of Janus nanosheets using a closely similar procedure,²⁵ two products with different stacking regularities, A-type and B-type, latter of which undergoing surface modification at both interlayers I and II, were obtained by changing the drying method. This phenomenon was enabled by exfoliation of the product into single-layered nanosheets in the reaction system. In the previous report, interlayer I was modified by octadecylphosphonic acid, and surface modification of interlayer II with carboxypropylphosphonic acid was conducted in THF. An affinity between these two surface modifier moieties and THF probably caused exfoliation in the second surface modification process. On the other hand, PPA_PA_NbO was obtained only as an A-type derivative, indi-

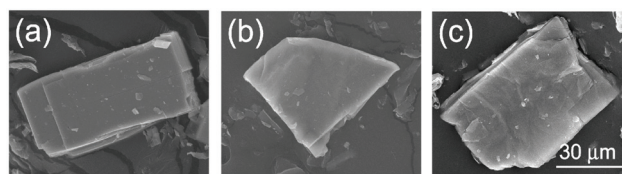


Fig. 4 SEM images of (a) K₄Nb₆O₁₇·3H₂O, (b) PPA_NbO and (c) PPA_PA_NbO.



cating that exfoliation did not occur in the surface modification process. This might suggest that the affinity between the PPA and PA moieties and 2-butanone was insufficient to cause exfoliation.

After ultrasonication of PPA_PA_NbO in water, a PPA_PA_NS aqueous dispersion was obtained. Fig. 5a shows a photograph of the PPA_PA_NS aqueous dispersion. The PPA_PA_NS aqueous dispersion exhibited Tyndall scattering, indicating that PPA_PA_NS nanosheets were dispersed in water. Fig. 5b shows a TEM image of PPA_PA_NS. A low-contrast sheet-like shape was observed and the corresponding ED pattern showed a spotted pattern. The d values of these spots were calculated as $d = 0.40$ nm, 0.25 nm, and 0.32 nm, and they were assignable to 200, 202, and 002 of $[\text{Nb}_6\text{O}_{17}]^{4-}$ nanosheets, respectively, since the lattice parameters of the original compound $\text{K}_4\text{Nb}_6\text{O}_{17}\cdot 3\text{H}_2\text{O}$ were $a = 0.80$ nm and $c = 0.64$ nm.¹⁶ This image was therefore assumed to be an exfoliated nanosheet, PPA_PA_NS nanosheets. Also, the lateral sizes of the nanosheets observed in Fig. 5b were about 700–800 nm, which was much smaller than the lateral size of the unexfoliated particle observed in the SEM image. Thus, the nanosheets after exfoliation seemed to be crushed by ultrasonication to form their smaller PPA_PA_NS nanosheets. A wide variation in the lateral sizes of PPA_PA_NS nanosheets was observed, which was likely caused by an uncontrolled braking process during ultrasonication for exfoliation.³⁰

Fig. 6 shows a typical AFM image of PPA_PA_NS casted on Si wafer. A sheet-like shape with a lateral dimension of about 1 μm was observed, and the thickness of the nanosheet was ~ 1.9 nm. The thickness of single-layered PPA_PA_NS was estimated by halving the repeating distance, obtained by XRD measurement, of PPA_PA_NbO with a A-type structure: 3.62 nm $\div 2 = 1.81$ nm. The thickness of a nanosheet observed by AFM, 1.9 nm, is closely similar to this value. It is worth emphasizing that the thickness value was not attributable to the double-layered nanosheets, in which the hydrophobic surfaces of two nanosheets stick to each other and the hydrophilic surfaces face outward on both sides. The dispersion state of

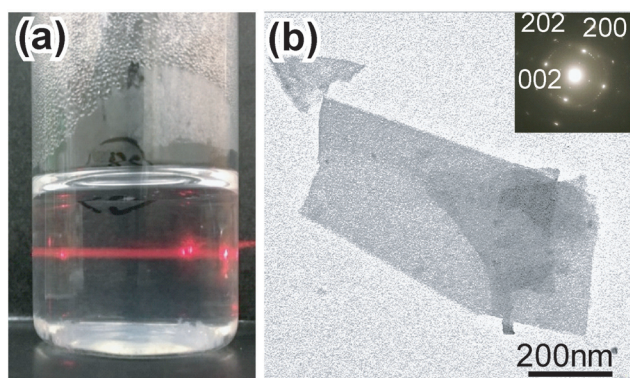


Fig. 5 (a) Photograph of PPA_PA_NS aqueous dispersion and (b) TEM image of PPA_PA_NS. Insertion is ED pattern corresponding to the TEM image.

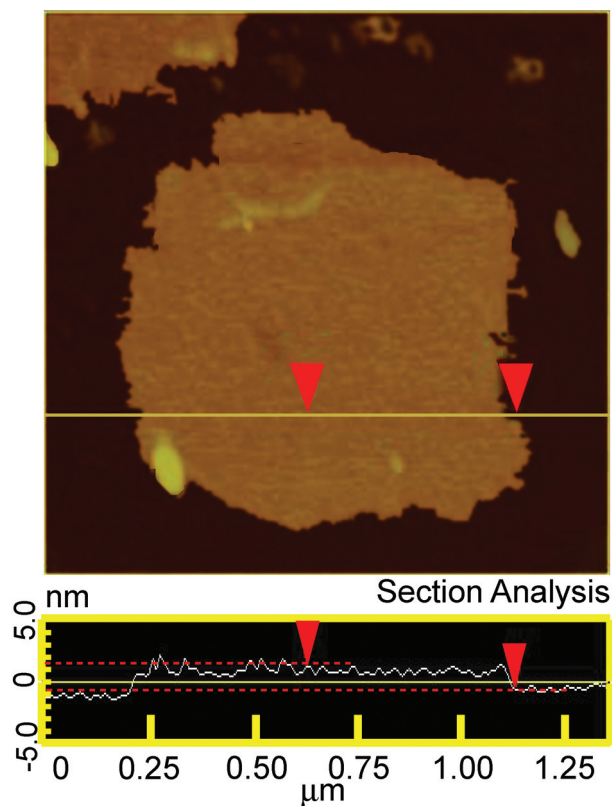


Fig. 6 AFM image of typical PPA_PA_NbO and height profile.

PPA_PA_NS nanosheets is ruled kinetically, not thermodynamically. Since single-layered PPA_PA_NS nanosheets have been observed by AFM imaging, single-layered nanosheets should be dominant in the experimental time scale. On the other hand, when the dispersion was allowed to stand for a few months, the PPA_PA_NS nanosheets were first aggregated and, finally, precipitated. It is therefore reasonable to assume the formation of aggregation with bilayer structures, whose amount should increase with time. Since the actual shapes of nanosheets are not uniform, some hydrophobic surface regions should still be exposed in the aggregation of bilayer structures. These remaining hydrophobic surface regions would promote additional stacking involving other nanosheets, and continuous stacking would lead to precipitation. It should be noted that this behaviour is directly related to the aggregation mechanism in the emulsion described later. Taking solid-state NMR and ICP results into consideration, it is concluded that single-layered water-dispersible Janus nanosheets modified with PA moieties on one side and PA moieties on the other side of the individual nanosheets were successfully prepared.

Surface behaviour of PPA_PA_NS nanosheets at the air-water interface: dynamic surface tension measurements

Based on the above results, it was expected that PPA_PA_NS nanosheets, which had two surfaces, a hydrophobic surface dominantly modified using the PPA moiety and a hydrophilic



surface modified with the PA moiety, could act as a two-dimensional surfactant. The surface behaviour of PPA_PA_NS nanosheets was therefore investigated by surface tension measurement. Fig. 7 shows the results of dynamic surface tension measurements of water, a PPA aqueous solution (1 mg L⁻¹), a PPA_PA_NS aqueous dispersion (1 mg L⁻¹), and a C₁₂NCl aqueous solution (0.19 mg L⁻¹). PPA (Fig. 7b, with this concentration) did not reduce the surface tension effectively, and the surface tension curve was very similar to that of water (Fig. 7a). It was considered that PPA was stably dissolved in water and that PPA molecules were not present at the air–water interface. On the other hand, the PPA_PA_NS aqueous dispersion (Fig. 7c) affected the surface tension, which gradually decreased with time, becoming 59.5 mN m⁻¹ after 20 000 s. Since PPA_PA_NS nanosheets reduced the surface tension, it is concluded that PPA_PA_NS nanosheets behaved as a two-dimensional surfactant. PPA_PA_NS nanosheets can be considered to be a two-dimensional assembly of PPA molecules, which do not show surface activity by themselves. It is thus likely that assembly of PPA and PA moieties on the nanosheet surfaces provided sufficient hydrophilicity on one side and hydrophobicity on the other side of the individual nanosheets, leading to the occurrence of surface activity. The PPA_PA_NS nanosheets required a much longer period of time to reduce surface tension than conventional surfactants, moreover, which normally require several seconds to decrease surface tension.³¹ In a previous study of surface behaviour of a protein at an air–water interface, β-casein, a protein with a much larger molecular weight of about 24 000 as compared to those of conventional surfactants, required a period of over 1000 s to decrease surface tension, probably because the protein molecules moved slowly to the air–water interface due to the protein's large molecular weight.³² Assuming that a PPA_PA_NS

nanosheet is a square plate with a 1.0 μm lateral size based on its AFM image (Fig. 6), the weight of a PPA_PA_NS nanosheet is calculated to be 7.0 × 10⁻¹⁵ g, which is heavier than nanosheets comprising hexaethylene glycol mono hexadecyl ether, a typical molecular surfactant, or β-casein, whose weights were calculated at 8.4 × 10⁻²² g and 4.0 × 10⁻²⁰ g, respectively.^{31,32} Thus, PPA_PA_NS nanosheets were expected to move more slowly than conventional surfactants, with a longer period of time was required to decrease surface tension in the PPA_PA_NS aqueous dispersion. It should be also noted that it took about 1000 s for the decrease in surface tension in the PPA_PA_NS aqueous dispersion to begin. Similar phenomena were reported in systems using surfactants with large molecular weights, such as gemini and polymeric surfactants,³³ and were ascribable to slow diffusion to and orientation toward the air–water interfaces. The relatively long induction period observed for the aqueous dispersion of PPA_PA_NS nanosheets would also be due to their extremely heavy weights compared to conventional surfactants.

On the other hand, the surface tension after 60 s from the start of measurement was 64.6 mN m⁻¹, which was lower than that of water, as shown in Fig. 4a; the PPA_PA_NS aqueous dispersion had already decreased surface tension in 60 s. The surface tension of C₁₂NCl aqueous solution (Fig. 7d) was reduced to 50.7 mN m⁻¹ at the start of the measurement. It should be noted that the amount of C₁₂N⁺ in this C₁₂NCl aqueous solution was adjusted to that of the C₁₂N⁺ ions remaining on the PPA_PA_NS nanosheet surface, the amount corresponding to the molar ratio of Nb : N = 6.0 : 1.0 based on ICP and CHN elemental analysis results (Table 1). It is thus likely that part of the C₁₂N⁺ ions were desorbed from the PPA_PA_NS nanosheet surface and that they moved quickly to the interface upon dispersion of PPA_PA_NS nanosheets in water to decrease the surface tension of the PPA_PA_NS aqueous dispersion immediately after the start of surface tension measurement.

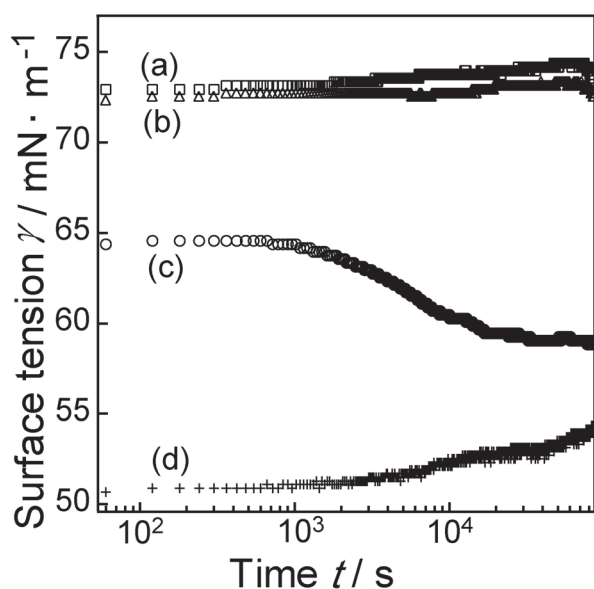


Fig. 7 Dynamic surface tension of (a) water, (b) PPA aqueous solution, (c) PPA_PA_NS aqueous dispersion and (d) C₁₂NCl aqueous solution.

Effect of PPA_PA_NS nanosheets at water-toluene interfaces: time evolution of toluene droplets in a PPA_PA_NS aqueous dispersion/toluene emulsion

The previous section has clearly demonstrated that PPA_PA_NS nanosheets can act as a two-dimensional surfactant at the water–air interface. In this section, behaviour of PPA_PA_NS nanosheets at a water–toluene interface is discussed based on optical microscope observation of an o/w emulsion.

The o/w emulsion was prepared using a PPA_PA_NS aqueous dispersion and toluene coloured by oil orange through ultrasonication. Fig. 8 shows photographic images of the PPA_PA_NS aqueous dispersion and toluene before and after ultrasonication. Before ultrasonication (Fig. 8a), the PPA_PA_NS aqueous dispersion (lower phase) and toluene (upper phase) were separated. After ultrasonication (Fig. 8b), a white suspension was formed, indicating that emulsification had proceeded. In Fig. 8b, the excess toluene which was not emulsified remained as an orange portion. Similar emulsifica-



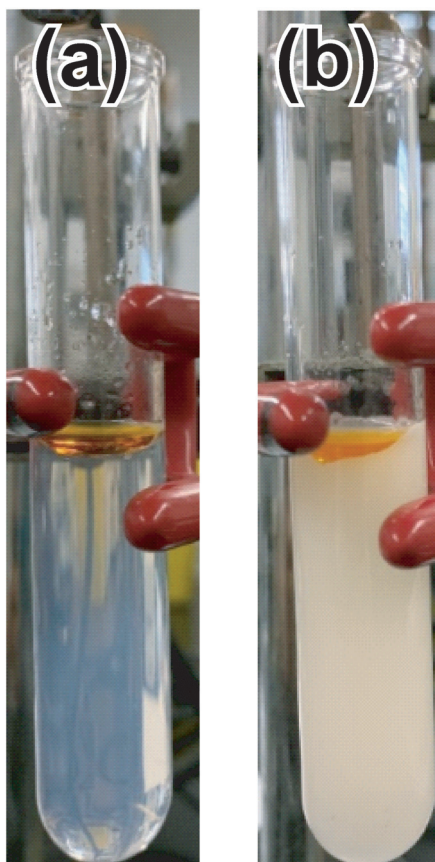


Fig. 8 PPA_PA_NS aqueous dispersions and toluene (a) before and (b) after ultrasonication. Under these conditions, the over half of toluene was emulsified with 10 mL of PPA_PA_NS aqueous dispersion. Thus, emulsion efficiency was calculated as follows; 0.1–0.2 mL (of toluene)/10 mL (of PPA_PA_NS aqueous dispersion) = 1–2 v/v%.

tion tests were conducted using toluene and one of two types of aqueous dispersions containing hexaniobate nanosheets which were modified symmetrically (a type prepared using PPA only and another prepared using PA only). No stable emulsions were formed using symmetrical nanosheets, although PPA_PA_NS nanosheets stabilized an emulsion. These observations demonstrate that the adsorption of PPA_PA_NS nanosheets at the water–toluene interface is based on a Janus structure. This result is supported by contact angle measurement using model substrates (see Tables S1 and S2†).

PPA_PA_NS nanosheets on the surfaces of oil droplets may possess a bending capability to adjust the curvatures of the oil droplets, according to the correlation between the sizes of the droplets and nanosheets. It should be noted that nanosheets with atomic thicknesses are flexible. In a previous report,³⁴ roll-ups of hexaniobate nanosheets with 20–40 nm axis diameters were observed.

Fig. 9 shows optical microscopic images of the PPA_PA_NS aqueous dispersion/toluene emulsion at the start of measurement, and after 1500, 2640 and 3600 s at room temperature. A movie of this observation is also available as ESI (Movie S1,† Reproduction speed is 12 times faster than real speed.).

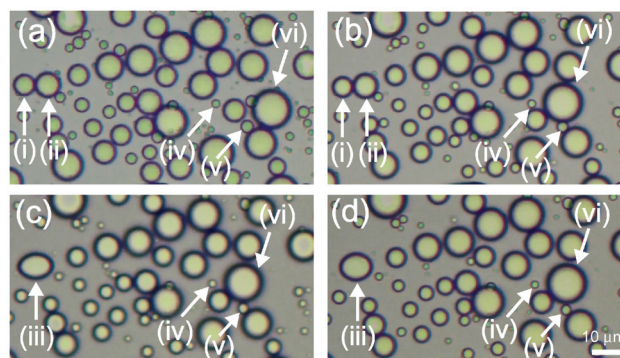


Fig. 9 Optical microscope images of the toluene/PPA_PA_NS aqueous dispersion emulsion; (a) at time of starting measurement (0 s), (b) after 1500 s, (c) after 2640 s and (d) after 3600 s.

Toluene droplets coloured by oil orange were observed, and the formation of an o/w emulsion was clearly demonstrated. The total number of toluene droplets in Fig. 9a, the image of the as-prepared emulsion, was 114. After 3600 s, meanwhile, the total number of toluene droplets in the same frame (Fig. 9d) had decreased to 78. A closer look at the images suggests that coalescence and Ostwald ripening occurred, and the details are described below.

Coalescence process of toluene droplets covered with PPA_PA_NS nanosheets

Enlarged views of toluene droplets (i), (ii) and (iii) in Fig. 9 are shown in Fig. 10. Toluene droplets (i) and (ii) in Fig. 10a and b coalesced and formed a toluene droplet (iii) with a non-spheri-

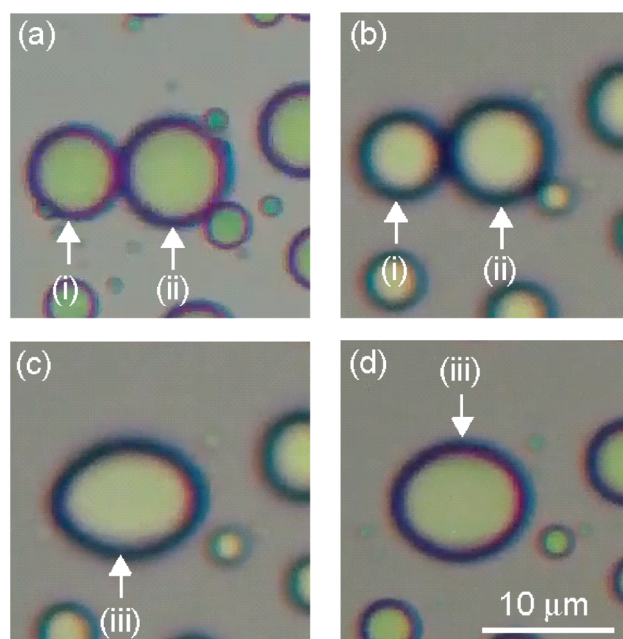


Fig. 10 Enlarged views of toluene droplets (i), (ii) and (iii) in Fig. 9 after (a) 0 s, (b) 2617 s, (c) 2618 s and (d) 3602 s.



Table 2 Sphericity of toluene droplet (iii) in Fig. 10b and Fig. 10d

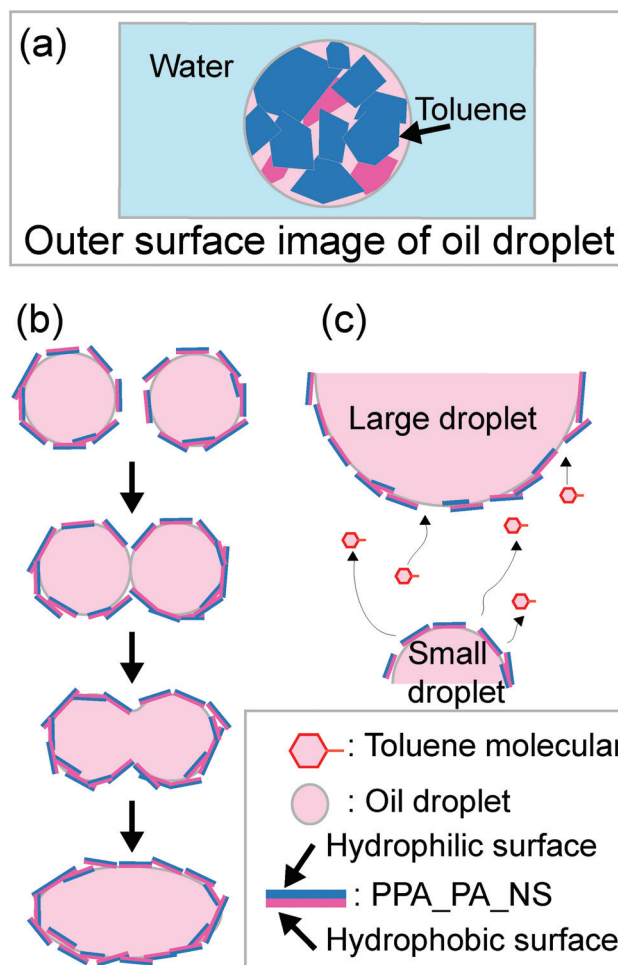
Time/s	Sphericity/–
2617	0.88
3602	0.91

cal shape in Fig. 10c and d. It took only 1 s for coalescence of toluene droplets (i) and (ii) to form a single toluene droplet (iii) (between Fig. 10b and c). On the other hand, the formed toluene droplet (iii) maintained a non-spherical ellipsoidal shape for 984 s, and the shape changed from a non-spherical shape toward a truly spherical shape over time (Fig. 10c and d); the sphericity of toluene droplet (iii) gradually increased from 0.88 to 0.91 during this time period (Table 2). This was not exceptional behaviour, since similar coalescence of non-spherical toluene droplets is also observed at other droplet in Movies S2, S3 and S4,† whose reproduction speed is 12 times faster than real speed, corresponding enlarged views were shown in Fig. S1, S2 and S3.†

Conventional surfactants cover interfaces of droplets in o/w emulsions perfectly, and these oil droplets are immediately transformed into perfect spherical shapes after coalescence.³⁵ The toluene droplets with non-spherical shapes in the emulsion observed in the present study should be due to the formation and immobilization of shells (multilayers) consisting of partially stacked PPA_PA_NS nanosheets at the toluene-water interface, as shown in Scheme 2. The non-spherical shapes of the droplets in an emulsion also exhibit a similarity to “liquid marbles”, liquid droplets wrapped by powders with non-spherical shapes, rather than to the ordinary spherical droplets of emulsions.^{36,37} Note that a PPA_PA_NS nanosheet dispersion is relatively stable in a homogeneous aqueous solution. Therefore, the driving force behind the multilayer formation must be an increased concentration of PPA_PA_NS nanosheets caused by additional adsorption onto PPA_PA_NS nanosheets at the toluene-water interface. These multilayer arrangements of PPA_PA_NS nanosheets likely inhibited rapid deformation of the toluene droplets, and the transitional shapes of coalesced toluene droplets could be observed in the emulsion for more than 600 s (Scheme 2b). It is considered that the stacking process proceeded further for the rearrangement of surfactants when the toluene droplets fused, in particular, and that the resulting toluene droplet with a distorted form was fixed. Similar phenomena, the formation of non-spherical droplets in emulsions, have been reported for emulsions prepared using graphene oxide nanosheets.^{38,39}

Ostwald ripening process of toluene droplets covered with PPA_PA_NS nanosheets

The sizes of toluene droplets (iv), (v) and (vi) in Fig. 9d were changed from those in Fig. 9a. Enlarged views of these toluene droplets are shown in Fig. 11. As observed in Fig. 11, the sizes of toluene droplets (iv) and (v) decreased and the size of toluene droplet (vi) increased during the optical microscopic observation. In Fig. 11a, the diameters of toluene droplets (iv)



Scheme 2 Schematic illustrations of (a) surface of toluene droplet, (b) coalescence process, and (c) Ostwald ripening process of toluene droplets covered by PPA_PA_NS nanosheets.

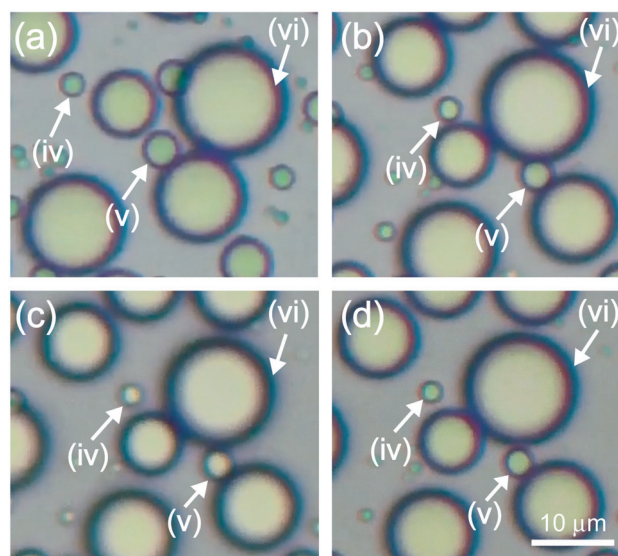


Fig. 11 Enlarged view of toluene droplets (iv), (v) and (vi) in Fig. 9 at (a) 0 s, (b) 1500 s, (c) 2640 s and (d) 3600 s.



and (v) were 4.7 and 3.1 μm , respectively, while the diameters of toluene droplets (iv) and (v) in Fig. 11d decreased to 2.8 and 2.3 μm , respectively. At the same time, the diameter of the large toluene droplet (vi) near toluene droplets (iv) and (v) increased slightly from 14.2 μm in Fig. 11a to 14.3 μm in Fig. 11d. This phenomenon, a reduction in the diameters of the small droplets and an increase in the diameter of the large droplet, is ascribable to Ostwald ripening. It is generally accepted that Ostwald ripening of emulsions stabilized with conventional molecular nonionic and ionic surfactants proceeds slowly, with the theoretical ripening rate of emulsions calculated as $9.2 \times 10^{-22} \text{ m}^3 \text{ s}^{-1}$.⁴⁰ The size change in the toluene droplets in the present PPA_PA_NS aqueous dispersion/toluene emulsion, on the contrary, proceeded within 3600 s during optical microscopic observation, indicating that Ostwald ripening in the present system proceeded significantly faster than that observed for conventional surfactant systems. It was reported that Ostwald ripening of a Pickering emulsion stabilized by silica nanoparticles was faster than that of one stabilized by a conventional surfactant, and that the ripening rate was about $10^{-18} \text{ m}^3 \text{ s}^{-1}$.³⁸ It was proposed that Ostwald ripening proceeded rapidly when oil molecules were dissolved from gaps between silica nanoparticles on small toluene droplets to the aqueous phase, with subsequent dissolved through gaps with a ripening rate of about $1.2 \times 10^{-20} \text{ m}^3 \text{ s}^{-1}$, as calculated from the changes in the molecular diffusion into larger toluene droplets. In the emulsion stabilized by PPA_PA_NS nanosheets, it is probable that nanosheets cannot cover the toluene droplet surface completely despite likely formation of PPA_PA_NS nanosheet multilayer arrangements. Thus, toluene molecules would be diameters of toluene droplets (iv), (v) and (vi) in Fig. 11, which are faster than those of conventional molecular surfactants (Scheme 2c). The Ostwald ripening of toluene droplets can therefore be observed in a short period of time. The dynamic behaviour and adsorption states of Janus nanosheets at the air–water interface and water–toluene interface cannot be estimated precisely, however, because information on their adsorption state remains limited.

Conclusions

Water-dispersible Janus nanosheets with surface activity were successfully prepared by the suitable selection of hydrophobic PPA and hydrophilic PA as surface modifiers. A Janus nanosheet aqueous dispersion was obtained by two-step sequential regioselective interlayer surface modification of $\text{K}_4\text{Nb}_6\text{O}_{17} \cdot 3\text{H}_2\text{O}$ using PPA and PA and subsequent exfoliation by ultrasonication in water to form single-layered nanosheets. The dispersion using a 2-D surfactant exhibited multiple characteristic behaviours due to the shape and large weight of the single-layered nanosheets; Janus PPA_PA_NS nanosheets reduced the surface tension of water slowly over a very long period of time, and in an o/w emulsion prepared using a Janus PPA_PA_NS nanosheet aqueous dispersion and toluene, a non-spherical toluene droplet and rapid Ostwald ripening were

observed. These results clearly demonstrate that our strategy is capable of preparing single-layered water-dispersible Janus PPA_PA_NS nanosheets which act as a two-dimensional surfactant and of clarifying the characteristics of their surface and interfacial behaviour. Although further investigation of the behaviour of Janus nanosheets on air–water and various water–organic solvent interfaces will be required to improve their performances, Janus nanosheets clearly offer enormous potential as two-dimensional surfactants that form emulsions with various water–organic solvent combinations and adjust their dynamic surface tension by changing their immobilized functional groups and lateral sizes.

Conflicts of interest

There are no conflicts to declare.

Acknowledgements

This work was supported by JSPS KAKENHI Grant Number 20K21241.

References

- 1 E. A. Calderon, V. B. Medrano and M. A. Guzmán, in *Fundamentals of Nanoparticles*, ed. A. Barhoum and A. S. H. Makhlof, Elsevier, Amsterdam, 2018, ch. 3, pp. 51–70.
- 2 J. H. Park, D. S. Dumani, A. Arsiwala, S. Emelianov and R. S. Kane, *Nanoscale*, 2018, **10**, 15365–15370.
- 3 F. Tu and D. Lee, *J. Am. Chem. Soc.*, 2014, **136**, 9999–10006.
- 4 M. Lattuada and T. A. Hatton, *Nano Today*, 2011, **6**, 286–308.
- 5 Y. Sheng, X. Yang, N. Yana and Y. Zhu, *Soft Matter*, 2013, **9**, 6254–6262.
- 6 Y. Nonomura, S. Komura and K. Tsujii, *Langmuir*, 2004, **20**, 11821–11823; Y. Nonomura, S. Komura and K. Tsujii, *J. Phys. Chem. B*, 2006, **110**, 13124–13129.
- 7 B. P. Binks, *Phys. Chem. Chem. Phys.*, 2007, **9**, 6298–6299.
- 8 B. P. Binks and P. D. I. Fletcher, *Langmuir*, 2001, **17**, 4708–4710.
- 9 R. Aveyard, *Soft Matter*, 2012, **8**, 5233–5240.
- 10 P. Raffa, D. A. Z. Wever, F. Picchioni and A. A. Broekhuis, *Chem. Rev.*, 2015, **115**, 8504–8563.
- 11 M. Nitschke and S. G. V. A. O. Costa, *Trends Food Sci. Technol.*, 2007, **18**, 252–259.
- 12 L. E. Low, S. P. Siva, Y. K. Ho, E. S. Chan and B. T. Tey, *Adv. Colloid Interface Sci.*, 2020, **277**, 102117.
- 13 B. P. Binks, *Curr. Opin. Colloid Interface Sci.*, 2002, **7**, 21–41.
- 14 G. Liu, J. Tian, X. Zhang and H. Zhao, *Chem. – Asian J.*, 2014, **9**, 2597–2603.
- 15 H. Jia, J. Dai, P. Huang, Y. Han, Q. Wang, J. He, J. Song, X. Wei, H. Yan and D. Liu, *Energy Fuels*, 2020, **34**, 13977–13984.
- 16 D. Gao, M. Zhang, B. Lyu, J. Ma and Y. Li, *Colloids Surf., A*, 2020, **607**, 125295.



- 17 S. Xie, S. Chen, Q. Zhu, X. Li, D. Wang, S. Shen, M. Jin, G. Zhou, Y. Zhu and L. Shui, *ACS Appl. Mater. Interfaces*, 2020, **12**, 26374–26383.
- 18 D. Xue, X. Song and F. Liang, *RSC Adv.*, 2017, **7**, 25450–25454.
- 19 X. Ji, Q. Zhang, F. Liang, Q. Chen, X. Qu, C. Zhang, Q. Wang and J. Li, *Chem. Commun.*, 2014, **50**, 5706–5709.
- 20 Q. B. Meng, P. Yang, T. Feng, X. Ji, Q. Zhang, D. Liu, S. Wu, F. Liang, Z. Zheng and X. Song, *J. Colloid Interface Sci.*, 2017, **507**, 74–82.
- 21 X. Zhang, H. Ren and A. He, *Nanoscale*, 2018, **10**, 19351–19359.
- 22 D. Luo, F. Zhang, H. Zheng, Z. Ren, L. Jiang and Z. Ren, *Chem. Commun.*, 2019, **55**, 1318–1321.
- 23 S. Zhao, L. Li, H. Zhang, B. Qian, J. Luo, Z. Deng, S. Shi, T. P. Russellcde and Z. Yu, *Mater. Chem. Front.*, 2020, **4**, 910–917.
- 24 L. Zhang, Q. Lei, J. Luo, M. Zeng, L. Wang, D. Huang, X. Wang, S. Mannan, B. Peng and Z. Cheng, *Sci. Rep.*, 2019, **9**, 163.
- 25 R. Suzuki, M. Sudo, M. Hirano, N. Idota, M. Kunitake, T. Nihimi and Y. Sugahara, *Chem. Commun.*, 2018, **54**, 5756–5759; R. Suzuki, M. Sudo, M. Hirano, N. Idota, M. Kunitake, T. Nihimi and Y. Sugahara, in *Functional Materials [On line]*, ed. E. R. Sahu, IntechOpen, London, 2019, ch. 3; R. Suzuki, N. Idota, T. Nishimi and Y. Sugahara, *Chem. Lett.*, 2020, **49**, 1058–1061.
- 26 N. Kimura, Y. Kato, R. Suzuki, A. Shimada, S. Tahara, T. Nakato, K. Matsukawa, P. H. Mutin and Y. Sugahara, *Langmuir*, 2014, **30**, 1169–1175.
- 27 F. A. Pavan, M. S. P. Francisco, R. Landers and Y. Gushikem, *J. Braz. Chem. Soc.*, 2005, **16**(4), 815–820.
- 28 T. Sugaya, M. Ozaki, R. Guégan, N. Idota and Y. Sugahara, *Langmuir*, 2019, **35**, 6594–6601.
- 29 R. Kaito, K. Kuroda and M. Ogawa, *J. Phys. Chem. B*, 2003, **107**, 4043–4047.
- 30 N. Miyamoto and T. Nakato, *J. Phys. Chem. B*, 2004, **108**, 6152–6159.
- 31 B. V. Zhmud, F. Tiberg and J. Kizling, *Langmuir*, 2000, **16**, 2557–2565.
- 32 R. Miller, V. B. Fainerman, E. V. Aksenenko, M. E. Leser and M. Michel, *Langmuir*, 2004, **20**, 771–777.
- 33 P. Raffa, D. A. Z. Wever, F. Picchioni and A. A. Broekhuis, *Chem. Rev.*, 2015, **115**, 8504–8563.
- 34 Y. Kobayashi, H. Hata, M. Salama and T. E. Mallouk, *Nano Lett.*, 2007, **7**, 2142–2145.
- 35 I. B. Ivanov and P. A. Kralchevsky, *Colloids Surf., A*, 1997, **128**, 155–175.
- 36 F. Geyer, Y. Asami, D. Vollmer, H.-J. Butt, Y. Nakamura and S. Fujii, *Adv. Funct. Mater.*, 2019, **29**, 1808826.
- 37 S. Fujii and R. Murakami, *KONA Powder Part. J.*, 2008, **26**, 153–166.
- 38 P. Wei, Q. Luo, K. J. Edgehouse, C. M. Hemmingsen, B. J. Rodier and E. B. Pentzer, *ACS Appl. Mater. Interfaces*, 2018, **10**, 21765–21781.
- 39 T. M. Ruhland, A. H. Gröschel, N. Ballard, T. S. Skelhon, A. Walther, A. H. E. Müller and S. A. F. Bon, *Langmuir*, 2013, **29**, 1388–1394.
- 40 J. A. Juárez and C. P. Whitby, *J. Colloid Interface Sci.*, 2012, **368**, 319–325.

